

The intensification of winter mid-latitude storm tracks in the Southern Hemisphere

Rei Chemke¹ & Yi Ming² & Janni Yuval³

¹*Department of Earth and Planetary Sciences, Weizmann Institute of Science, Rehovot, Israel*

²*NOAA/Geophysical Fluid Dynamics Laboratory, Princeton, New Jersey, USA*

³*Department of Earth, Atmospheric and Planetary Sciences, MIT, Cambridge, Massachusetts, USA*

The strength of mid-latitude storm tracks shapes weather and climate phenomena in the extra-tropics, as these storm tracks control the daily to multi-decadal variability of precipitation, temperature and winds. By the end of this century, winter mid-latitude storms are projected to intensify in the Southern Hemisphere, with large consequences over the entire extra-tropics. Therefore, it is critical to be able to accurately assess the impacts of anthropogenic emissions on these storms, in order to improve societal preparedness for future changes. Here we show that current climate models severely underestimate the intensification in mid-latitude storm-tracks in recent decades. Specifically, the intensification obtained from reanalyses has already reached the model-projected end of the century intensification. The biased intensification is found to be linked to biases in the zonal flow. These results question the ability of climate models to accurately predict the future impacts of anthropogenic emissions in the Southern Hemisphere mid-latitudes.

Corresponding author: Rei Chemke¹; Email: rei.chemke@weizmann.ac.il

Main

Mid-latitude storms transfer momentum, moisture and heat across different latitudes and longitudes, thus controlling the distribution of winds, precipitation and temperature over the extra-tropics¹⁻⁴. By the end of this century, climate models project a robust strengthening of winter mid-latitude storms in the Southern Hemisphere⁵⁻¹³, which will have large climate consequences for the entire Southern Hemisphere extra-tropics^{14, 15}.

Over the 1980-2012 period, Southern Hemisphere winter cyclones were also found to intensify in one reanalysis¹⁶. However, whether this recent strengthening of winter mid-latitude storms is part of the emerged forced response or merely part of internal climate variability is still an open question. The answer to this question will reveal part of the impacts of anthropogenic emissions on the mid-latitude circulation in recent decades, which will allow policymakers to construct more accurate adaption strategies. Another motivation for investigating the recent changes in the mid-latitude flow comes from previous studies who documented model biases in the climatological (time mean) Southern Hemisphere winter circulation, including an equatorward bias in the climatological position of the mean zonal wind¹⁷⁻¹⁹, and an underestimation of the climatological strength of high-intensity cyclones²⁰. Thus, investigating the recent changes in the intensity of wintertime mid-latitude storms in models will also allow us to evaluate how well climate models reproduce the trends of mid-latitude storms over the last decades, and potentially discover biases in the projections of storms in current climate models. We here focus on intensity changes of the storm tracks during winter, since during summer, the storm tracks are projected to shift poleward, which results in minor changes in their mid-latitude mean intensity¹⁰.

Recent trends in Southern Hemisphere winter storm tracks

We start by examining the recent changes in the intensity of Southern Hemisphere winter (June-August; results for September-November are shown in Supplementary Fig. 1) mid-latitude storm tracks using the transient eddy kinetic energy (EKE, Methods^{6,8,21,22}). Specifically, we focus on the 40-year trends (1979-2018) of mid-latitude EKE in 3 different reanalyses and 16 models (Fig. 1a) that participate in the Coupled Model Intercomparison Project Phase 6²³ (CMIP6), forced with the Historical and the SSP5-8.5 future scenario (Methods). We find that in reanalyses, the EKE have intensified over the last four decades in a mean rate of $1.8 \times 10^3 \text{ Jm}^{-2}\text{yr}^{-1}$ (blue bar; varying between $1.4 \times 10^3 - 2.5 \times 10^3 \text{ Jm}^{-2}\text{yr}^{-1}$ across the reanalyses, black circles)¹⁶. In contrast, CMIP6 models simulate a much weaker strengthening, which varies across the models between $-315 \text{ Jm}^{-2}\text{yr}^{-1}$ and $570 \text{ Jm}^{-2}\text{yr}^{-1}$ (black circles), with a multi-model mean value of $210 \text{ Jm}^{-2}\text{yr}^{-1}$ (gray bar). Thus, not a single model is able to capture the intensification of the EKE in reanalyses (not even when including the uncertainty in the mean reanalyses trend²⁴; black bar). This models-reanalyses discrepancy is not only evident over the entire 1979-2018 period, but also reanalyses show larger 10-, 20- and 30-year trends over the 1979-2018 period (Extended Data Fig. 1).

Examining the time evolution of EKE further reveals the large differences between reanalyses and climate models (Fig. 1b). First, climate models simulate a monotonic strengthening of the EKE over the 20th and 21st centuries⁵⁻¹³. In particular, over the last decade, the EKE in CMIP6 models has intensified by $\sim 2\%$ (with standard deviation of $\sim \pm 2\%$ across the models), relative to the 1980-1999 period, while in reanalyses the EKE have intensified by $\sim 12\%$; the percent changes are calculated relative to the baseline period of each model/reanalysis separately (the time

evolution of the different reanalyses is also shown in Supplementary Fig. 2). In CMIP6 models, a similar intensification by 12% is only projected to occur by 2080 (with standard deviation of ± 11 years across the models), which highlights that climate models may not only underestimate the recent storms' intensification, but might also severely under-predict the future intensification of the storms. Interestingly, the recent weakening of summer storms in the Northern Hemisphere in reanalyses was also found to occur in climate models only by the end of the 21st century²¹.

The intensification of the storm tracks also suggests a strengthening in the poleward eddy energy flux (flux by atmospheric perturbations, such as mid-latitude storms). To examine this we plot in Fig. 1c the 1979-2018 trends in wintertime poleward transient eddy moist static energy flux ($v'm'$, where v is meridional velocity, m is moist static energy and prime denotes eddy terms, Methods) at mid-latitudes; this energy flux accounts for the poleward eddy flux of heat, moisture and geopotential (Methods). Similar to the EKE trends, over the last four decades, $v'm'$ has intensified faster in reanalyses than in climate models; reanalyses show an intensification in a mean rate of $6 \times 10^{12} \text{ TWyr}^{-1}$, varying between $4.9 \times 10^{12} \text{ TWyr}^{-1}$ and $7 \cdot 10^{12} \text{ TWyr}^{-1}$ across the reanalyses, while CMIP6 models show a mean intensification of only $1 \times 10^{12} \text{ TWyr}^{-1}$, where not a single model is able to capture the intensification in the reanalyses. Decomposing the $v'm'$ trends reveals that the discrepancy between models and reanalyses is found in the poleward eddy heat and moisture fluxes, but not in the poleward eddy geopotential flux (Supplementary Fig. 3). Note that while it is conceivable that the larger trends in reanalyses might partly stem from larger climatological values, such direct relation is not found across models, nor across reanalyses (Supplementary Fig. 4). Moreover, while all reanalyses show larger EKE and $v'm'$ trends, some reanalyses have

similar climatological EKE and $v'm'$ values as in CMIP6 models.

Similar to the time evolution of EKE, $v'm'$ is also projected to monotonically intensify over the 21st century (Fig. 1d). In particular, over the last decade, climate models simulate a $\sim 4\%$ increase in $v'm'$ (with standard deviation of $\sim \pm 5\%$ across the models), relative to the 1980-1999 period, while reanalyses show a $\sim 16\%$ increase. A similar 16% increase in climate models is only projected to occur by 2070 (with standard deviation of ± 11 years across the models), which again stresses that climate models might under-predict the future changes in Southern Hemisphere eddy energy fluxes, and thus also their large impacts on the distribution of climate zones in the extra-tropics. Lastly, note that biases in long-term trends (and climatology²⁵) might be found in reanalyses²⁶, due to the inclusion of new observed products and data assimilation methods. However, the use of several reanalyses, which all show very similar monotonic increase in EKE and $v'm'$ over the last four decades, together with the fact that the larger 1979-2018 trends in reanalyses, relative to models, are evident also on shorter trends (Extended Data Fig. 1), provide us confidence to use these datasets to evaluate the recent changes in the storm tracks' activity.

Detection analysis for winter storm tracks intensification

Does the large discrepancy between reanalyses and climate models hinder the detection of the intensification of winter storm tracks in climate models? To answer this question we follow previous studies²⁷⁻²⁹ and analyze the time of emergence of the intensification, out of the internal climate variability, in both reanalyses and models. This is done using a signal-to-noise ratio approach, where the signal is defined as trends of different lengths, all starting from 1979 (the first year of the reanalyses). The noise is defined as two standard deviations of all trends, with the same length

as the signal, that arise only due to internal variability (estimated from pre-industrial control runs, Methods). The time of emergence is defined as the year when the signal (i.e., the trend) exceeds the noise.

In order to use the signal-to-noise ratio approach we first ensure that climate models adequately capture the internal variability of the storm tracks' trends, and thus can be used to assess the 'noise'. To compare the internal variability of the trends we calculate the standard deviation across all 10-year, 20-year and 30-year trends in models and reanalyses over the detrended 1979-2018 period. Similarly, we calculate the standard deviation across all trends of the same length from the pre-industrial control runs. We find that reanalyses and climate models have similar 10-, 20- and 30-year trends variability (Extended Data Fig. 3). Thus, climate models can be used to evaluate the internal variability of the storm tracks' trends.

The time of emergence of the intensification of mid-latitude EKE and $v'm'$ is shown in Fig. 2. The intensification signal of EKE in reanalyses emerged from the internal climate variability in the late '90s-early '00s (Fig. 2a). In contrast, the weaker strengthening in climate models significantly delays the emergence of the signal; the EKE intensification will emerge around 2050 in the multi-model mean, with standard deviation of ± 14 years. Similarly, the strengthening of $v'm'$ in reanalyses emerged around 2010 (Fig. 2b), while the emergence in climate models is projected to occur only around 2055 in the multi-model mean with standard deviation of ± 14 years. This highlights that, by underestimating the magnitude of the storm tracks' changes, climate models may also underestimate the timing of executing adaption and mitigation strategies in Southern Hemisphere mid-latitudes.

The source of the models-reanalyses discrepancy

Next, we examine three possible sources of the larger intensification of mid-latitude storm tracks in reanalyses, relative to models. First, the evolution of EKE and $v'm'$ in reanalyses is affected by both their response to external forcings and their internal variability^{24,30–32}. We thus start by examining whether the size of the CMIP6 ensemble analyzed here (i.e., 16 model trends) might not be large enough to capture the internal variability of 40-year trends, and thus also the trends in reanalyses (i.e., whether internal variability is mostly responsible for the strong trends in reanalyses). To evaluate the internal variability in 40-year EKE and $v'm'$ trends we calculate two standard deviations of all 40-year trends from the pre-industrial control runs²⁴ (total of 1961 and 1361 EKE and $v'm'$ trends, respectively), and center it around the multi-model mean 1979-2018 trend (red error bars on top of gray bars in Fig. 1a and 1c). While increasing the ensemble size does increase the range of CMIP6 EKE trends (compare red bars and black dots), even with a significantly larger ensemble size CMIP6 models still do not capture the recent trends in reanalyses (the overlap between the uncertainty in reanalyses $v'm'$ trends and the variability in the model trends suggests that internal variability could reduce, but not explain, the models' $v'm'$ bias^{24,32}; compare black and red error bars). Similarly, increasing the CMIP6 ensemble size by pooling together all 40-year trends over the 1969-2028 period (total of 320 trends), or examining the 1979-2018 trends using the Community Earth System Model (CESM) 40-member ensemble³³, where the spread across its members represents the internal variability (Methods), yields in similar results of smaller trends in models, relative to reanalyses (Supplementary Figs. 5-6). Thus, from the above analyses we conclude that the size of the CMIP6 ensemble is not likely to explain the smaller trends in models,

relative to reanalyses.

Second, the larger EKE and $v'm'$ trends in reanalyses, relative to models, might stem from the inability of climate models to simulate the recent cooling of the Southern Ocean surface³⁴. This model bias, was found to explain the models' inability to capture the recent trends in annual mean eddy heat fluxes²⁹. To evaluate the effect of recent observed changes in sea surface temperature (SST) in the models-reanalyses discrepancy we calculate the EKE and $v'm'$ trends using the Atmosphere Model Intercomparison Project Phase 6 (AMIP6) runs; in these runs there is no active ocean and sea-ice, and the SST and sea-ice are prescribed to observations (Methods). Although we find that correcting the simulated surface changes leads to slightly larger intensification in models, the intensification is relatively modest and we conclude that even AMIP6 runs do not capture the recent trends in reanalyses (green bars in Fig. 1a and 1c). This emphasizes that the inability of climate models to capture the recent wintertime EKE and $v'm'$ trends does not stem from biases in simulating SST trends. Interestingly, larger EKE trends, relative to AMIP6, are also found in NOAA-CIRES-DOE reanalysis (Supplementary Fig. 7), which, similar to AMIP6, uses observed SST and sea-ice, but, unlike AMIP6, it (only) assimilates surface pressure. This suggests, from geostrophic balance, that biases in the structure of the wind may affect the smaller EKE trends in models, relative to reanalyses (as further shown below).

Third, since mid-latitude eddies arise from hydrodynamic instability, we follow previous studies²², and further investigate the source of the models-reanalyses discrepancy by conducting a linear normal-mode instability analysis. Such analysis allows one to examine the (maximum) growth rate of mid-latitude eddies for a given mean atmospheric conditions, which represents the

extraction of energy from the mean flow by the eddies (Methods). In particular, we examine how changes in the vertical and meridional structures of the mean flow might explain the recent storm tracks changes, by modulating the eddy growth rate.

To examine the effect of changes in the vertical structure of the flow (i.e., baroclinicity), we conduct, at each year, a one-dimensional vertical linear normal-mode instability analysis to the quasi-geostrophic equations, using the mean zonal wind, static stability and tropopause height from each reanalysis and each model (Methods). Fig. 3a shows the two-dimensional probability density function of the CMIP6 1979-2018 EKE trends and the resulting growth rate trends (σ_{bc}), along with the corresponding trends in reanalyses (black dots). The EKE trends have low correlation with the growth rate trends across models ($r = 0.07$), and reanalyses not only show negative growth rate trends (which are inconsistent with the EKE trends, and stem from a reduced stability by the vertically dependent zonal flow and static stability), but also, in contrast to the EKE trends, reanalyses do not show larger σ_{bc} trends than the models. Examining simpler metrics for baroclinicity, such as the Eady growth rate or mean available potential energy (Methods), as was done in previous studies^{5-7,9,10}, yields similar results (Supplementary Fig. 8).

On the other hand, examining the link between EKE and the meridional structure of the mean flow (i.e., variations in the barotropic component of the flow), by conducting, using the tropospheric averaged mean zonal wind (\bar{u}), a one-dimensional meridional linear normal-mode instability analysis to the absolute vorticity equation (Methods), reveals that the EKE trends are correlated with the growth rate trends (σ_{bt}) across both models ($r = 0.63$) and reanalyses (Fig. 3b). Furthermore, similar to the EKE trends, reanalyses also show larger σ_{bt} trends than the models.

Similar results are found for the components of $v'm'$ (eddy heat and moisture fluxes, Supplementary Fig. 9). This suggests that although baroclinicity drives the formation of mid-latitude storms, here the changes in the storm tracks over recent decades, and the models-reanalyses discrepancy, seem to stem from the barotropic part of the flow. Note, that changes in the meridional structure of the flow might result in the models-reanalyses discrepancy by not only affecting the barotropic growth of mid-latitude eddies, but also their baroclinic growth via, for example, the barotropic governor³⁵, and by affecting the barotropic decay phase in eddy lifecycles³⁶.

To further demonstrate the different meridional structures of the wind in models and reanalyses, we next examine the 1979-2018 trends of the second meridional derivative of the mean zonal wind, $\frac{\partial^2 \bar{u}}{\partial y^2}$ (Extended Data Fig. 4), which plays an important role in the growth of eddies³⁷ (Methods). For example, in barotropic instability, positive values of $\frac{\partial^2 \bar{u}}{\partial y^2}$, which occur over the flanks of the zonal wind (the source regions for the instability), allows the necessary condition for instability to be met³⁷. Indeed, reanalyses exhibit an increase in $\frac{\partial^2 \bar{u}}{\partial y^2}$ over the equatorward and far-end poleward flanks of the wind, which might explain the increased growth rate in recent decades. In addition, an increase in eddy generation over the flanks of the jet also suggests convergence of momentum by the eddies ($-\frac{\partial \overline{u'v'}}{\partial y}$) over the flanks of the jet, that results in a double peak of $-\frac{\partial \overline{u'v'}}{\partial y}$ ^{38,39}. Such double peak behavior is also clearly evident in $-\frac{\partial \overline{u'v'}}{\partial y}$ trends in reanalyses (Extended Data Fig. 5). The increase in $\frac{\partial^2 \bar{u}}{\partial y^2}$ over the flanks of the jets and the double peak behavior of $-\frac{\partial \overline{u'v'}}{\partial y}$ are not captured in most CMIP6 models (Extended Data Figs. 4-5), which suggests that the effect of changes in recent decades in the meridional structure of the mean zonal wind on the eddy flow are smaller in climate models, relative to reanalyses, which might lead to the weaker EKE and $v'm'$

intensification.

Lastly, previous studies found model biases in the climatological position of the zonal wind^{17, 18} (which still exist, but have been improved, in CMIP6 models¹⁹) and were argued to affect the future meridional structure of the wind (i.e., the shift of the zonal flow). Thus, it is conceivable that such biases might also affect the model bias in EKE trends. However, third of the CMIP6 models used here show a poleward bias in the jet's latitude, relative to reanalyses, while the other two thirds an equatorward bias (Supplementary Fig. 10; while a larger set of models might result in a larger bias in the jet's position, still models show both poleward and equatorward biases¹⁹). Thus, since all models exhibit weaker EKE trends, relative to reanalyses, the different zonal wind positions are likely not the source of the EKE discrepancy; reanalyses and models exhibit different relations between jet latitude and EKE trends.

Discussion and conclusions

Using multiple reanalyses, we find that mid-latitude storm tracks, including their associated poleward energy flux, have substantially intensified over recent decades in response to external forcing. Climate models, on the other hand, are found here to significantly underestimate this intensification, which is only projected to occur in climate models by the late 21st century. The inability of climate models to adequately capture the storm tracks intensification, which delays the detection of the intensification in models by several decades, questions the skill of climate models to accurately assess the future changes in the Southern Hemisphere extra-tropics; mid-latitude storm tracks affect the distribution of heat, precipitation and weather events (including extreme events) from low subtropical regions to the high polar regions. We reveal that the biases in climate models

likely arise from biases in the meridional structure of the zonal flow, and not from a misrepresentation of internal variability in climate models nor from the models' inability to simulate the recent cooling in the Southern Ocean. Our analysis highlights the importance of further investigating observation-based data to assess both the impacts of human activity on mid-latitude climate, and the limitations in climate models (especially the biased zonal wind changes) to form accurate climate-change adaption and mitigation strategies for the Southern Hemisphere mid-latitudes.

Acknowledgements: R.C. is grateful to the WIS support of young scientists, and for Alexander Novosel-sky for downloading the data.

Author Contributions: R.C. analyzed the data and together with Y.M. and J.Y. discussed and wrote the paper.

Competing Interests: The authors declare that they have no competing interests.

References

1. Pfahl, S. & Wernli, H. Quantifying the Relevance of Cyclones for Precipitation Extremes. *J. Clim.* **25**, 6770–6780 (2012).
2. Catto, J. L., Madonna, E., Joos, H., Rudeva, I. & Simmonds, I. Global Relationship between Fronts and Warm Conveyor Belts and the Impact on Extreme Precipitation. *J. Clim.* **28**, 8411–8429 (2015).
3. Ma, C. G. & Chang, E. K. M. Impacts of Storm-Track Variations on Wintertime Extreme Weather Events over the Continental United States. *J. Clim.* **30**, 4601–4624 (2017).
4. Yau, A. M. W. & Chang, E. K. M. Finding Storm Track Activity Metrics That Are Highly Correlated with Weather Impacts. Part I: Frameworks for Evaluation and Accumulated Track Activity. *J. Clim.* **33**, 10169–10186 (2020).
5. Yin, J. H. A consistent poleward shift of the storm tracks in simulations of 21st century climate. *Geophys. Res. Lett.* **32**, L18701 (2005).
6. O’Gorman, P. A. Understanding the varied response of the extratropical storm tracks to climate change. *Proc. Natl. Acad. Sci. U.S.A.* **107**, 19176–19180 (2010).
7. Wu, Y., Ting, M., Seager, R., Huang, H. & Cane, M. A. Changes in storm tracks and energy transports in a warmer climate simulated by the GFDL CM2.1 model. *Clim. Dyn.* 203–222 (2010).
8. Chang, E. K. M., Guo, Y. & Xia, X. CMIP5 multimodel ensemble projection of storm track change under global warming. *J. Geophys. Res.* **117**, D23118 (2012).

9. Harvey, B. J., Shaffrey, L. C. & Woollings, T. J. Equator-to-pole temperature differences and the extra-tropical storm track responses of the CMIP5 climate models. *Clim. Dyn.* **43**, 1171–1182 (2014).
10. Lehmann, J., Coumou, D., Frieler, K., Eliseev, A. V. & Levermann, A. Future changes in extratropical storm tracks and baroclinicity under climate change. *Env. Res. Lett.* **9**, 084002 (2014).
11. Shaw, T. A. *et al.* Storm track processes and the opposing influences of climate change. *Nat. Geosci.* **9**, 656–664 (2016).
12. Chang, E. K. M. Projected Significant Increase in the Number of Extreme Extratropical Cyclones in the Southern Hemisphere. *J. Clim.* **30**, 4915–4935 (2017).
13. Blazquez, J. & Solman, S. A. Relationship between projected changes in precipitation and fronts in the austral winter of the Southern Hemisphere from a suite of CMIP5 models. *Clim. Dyn.* **52**, 5849–5860 (2019).
14. Bengtsson, L., Hodges, K. I. & Keenlyside, N. Will Extratropical Storms Intensify in a Warmer Climate? *J. Clim.* **22**, 2276 (2009).
15. Yettella, V. & Kay, J. E. How will precipitation change in extratropical cyclones as the planet warms? Insights from a large initial condition climate model ensemble. *Clim. Dyn.* **49**, 1765–1781 (2017).

16. Reboita, M. S., da Rocha, R. P., Ambrizzi, T. & Gouveia, C. D. Trend and teleconnection patterns in the climatology of extratropical cyclones over the Southern Hemisphere. *Clim. Dyn.* **45**, 1929–1944 (2015).
17. Kidston, J. & Gerber, E. P. Intermodel variability of the poleward shift of the austral jet stream in the CMIP3 integrations linked to biases in 20th century climatology. *Geophys. Res. Lett.* **37**, L09708 (2010).
18. Simpson, I. R. & Polvani, L. M. Revisiting the relationship between jet position, forced response, and annular mode variability in the southern midlatitudes. *Geophys. Res. Lett.* **43**, 2896–2903 (2016).
19. Bracegirdle, T. J. *et al.* Improvements in Circumpolar Southern Hemisphere Extratropical Atmospheric Circulation in CMIP6 Compared to CMIP5. *Earth Space Sci.* **7**, 01065 (2020).
20. Priestley, M. D. K. *et al.* An Overview of the Extratropical Storm Tracks in CMIP6 Historical Simulations. *J. Clim.* **33**, 6315–6343 (2020).
21. Coumou, D., Lehmann, J. & Beckmann, J. The weakening summer circulation in the Northern Hemisphere mid-latitudes. *Science* **348**, 324–327 (2015).
22. Chemke, R. & Ming, Y. Large atmospheric waves will get stronger, while small waves will get weaker by the end of the 21st century. *Geophys. Res. Lett.* **47**, e2020GL090441 (2020).
23. Eyring, V. *et al.* Overview of the Coupled Model Intercomparison Project Phase 6 (CMIP6) experimental design and organization. *Geosci. Model Dev.* **9**, 1937–1958 (2016).

24. Thompson, D. W. J., Barnes, E. A., Deser, C., Foust, W. E. & Phillips, A. S. Quantifying the Role of Internal Climate Variability in Future Climate Trends. *J. Clim.* **28**, 6443–6456 (2015).
25. Hodges, K., Cobb, A. & Vidale, P. L. How well are tropical cyclones represented in reanalysis datasets? *J. Clim.* **30**, 5243–5264 (2017).
26. Chemke, R. & Polvani, L. M. Opposite tropical circulation trends in climate models and in reanalyses. *Nat. Geosci.* **12**, 528–532 (2019).
27. Hawkins, E. & Sutton, R. Time of emergence of climate signals. *Geophys. Res. Lett.* **39**, L01702 (2012).
28. Santer, B. D. *et al.* Human and natural influences on the changing thermal structure of the atmosphere. *Proc. Natl. Acad. Sci. U.S.A.* **110**, 17235–17240 (2013).
29. Chemke, R. & Polvani, L. M. Linking polar amplification and eddy heat flux trends. *npj Clim. Atmos. Sci.* **3**, 8 (2020).
30. Hawkins, E. & Sutton, R. The Potential to Narrow Uncertainty in Regional Climate Predictions. *Bull. Am. Meteor. Soc.* **90**, 1095–1107 (2009).
31. Deser, C., Phillips, A., Bourdette, V. & Teng, H. Uncertainty in climate change projections: the role of internal variability. *Clim. Dyn.* **38**, 527–546 (2012).
32. Deser, C., Knutti, R., Solomon, S. & Phillips, A. S. Communication of the role of natural variability in future North American climate. *Nat. Clim. Change* **2**, 775–779 (2012).

33. Kay, J. E. *et al.* The Community Earth System Model (CESM) Large Ensemble Project: A Community Resource for Studying Climate Change in the Presence of Internal Climate Variability. *Bull. Am. Meteor. Soc.* **96**, 1333–1349 (2015).
34. Jones, J. M. *et al.* Assessing recent trends in high-latitude Southern Hemisphere surface climate. *Nat. Clim. Change* **6**, 917–926 (2016).
35. James, I. N. Suppression of Baroclinic Instability in Horizontally Sheared Flows. *J. Atmos. Sci.* **44**, 3710–3720 (1987).
36. Simmons, A. J. & Hoskins, B. J. The life cycles of some nonlinear baroclinic waves. *J. Atmos. Sci.* **35**, 414–432 (1978).
37. Vallis, G. K. *Atmospheric and Oceanic Fluid Dynamics* (pp. 770. Cambridge University Press, Cambridge, U.K., 2006).
38. Pedlosky, J. *Geophysical Fluid Dynamics* (2nd ed, pp. 710. New York, Springer-Verlag, 1987).
39. Kidston, J. & Vallis, G. K. Relationship between eddy-driven jet latitude and width. *Geophys. Res. Lett.* **37** (2010).

Methods

EKE

The Southern Hemisphere wintertime storm tracks' intensity is defined, following previous studies^{5–7,10,21}, as the column integrated June-August (JJA) transient eddy kinetic energy, $EKE = \frac{1}{g} \int_0^{p_s} u'^2 + v'^2 dp$, where g is gravity, p_s surface pressure, u and v are the zonal and meridional winds, respectively, p is pressure and prime denotes eddy terms, calculated using a bandpass filter of 2-6 days. Using a different bandpass filter to define the transient eddies (e.g., 3-10 days) yields similar results (Supplementary Fig. 11). We analyze here the column integrated mid-latitude mean (i.e., averaged zonally and over 40°S–70°S) EKE (as was done in previous studies^{6,8,21,22}) as the different intensification in models and reanalyses appears throughout the troposphere (Supplementary Fig. 12) and across most of the mid-latitudes (Supplementary Fig. 13).

Eddy moist static energy flux

The poleward transient eddy moist static energy flux is defined as $v'm' = \frac{2\pi a \cos \phi}{g} \int_0^{p_s} c_p \overline{v'T'} + L_v \overline{v'q'} + \overline{v'\Phi'} dp$, where $v'T'$, $v'q'$ and $v'\Phi'$ are the meridional eddy heat, moisture and geopotential fluxes, respectively, T is temperature, q is specific humidity, Φ is geopotential, overbar denotes zonal mean, $c_p = 1004 \text{ Jkg}^{-1}\text{K}^{-1}$ is specific heat capacity and $L_v = 2.5 \cdot 10^6 \text{ Jkg}^{-1}$ is latent heat of vaporization.

CMIP6 models

We use daily and monthly output from 16 models that participate in the Coupled Model Intercomparison Project Phase 6²³ (CMIP6, Supplementary Table 1; we use all models that have available daily data for the analysis), and in order to weigh all models equally, we select only the 'r1i1p1f1'

member in four experiments: historical (through 2014), future scenario SSP5-8.5 (through 2100), historical with prescribed SST and sea-ice (AMIP6, through 2014), and pre-industrial control run (with constant 1850 forcings). The constant external forcings in the control run allows one to evaluate the internal climate variability. Following previous studies²⁸, before assessing the internal climate variability, we first concatenate the detrended last 200 years of each model’s pre-industrial run, which yields $\sim 2,000$ years of control data. Lastly, we here use the long pre-industrial runs to assess the internal climate variability, rather than reanalyses data, since the length of the control runs not only allows one to gather enough statistics to adequately evaluate the internal variability, but also to account for the variability of 40-year trends, which cannot be estimated in reanalyses (as there is only one trend over the 1979-2018 period).

Reanalyses

Reanalyses provide the best approximation for the state of the atmosphere, as they assimilate air and surface observations in general circulation models, and thus are used here to examine the recent changes in mid-latitude storm tracks. Four reanalyses are examined in this study including JRA-55⁴⁰, NCEP2⁴¹, Era-Interim⁴² and NOAA-CIRES-DOE⁴³. We here analyze the Era-Interim, rather than ERA5⁴⁴, for consistency with the large body of work done using Era-Interim; nevertheless, similar results are also evident in ERA5 (Supplementary Fig. 14). Unlike the other reanalyses, the NOAA-CIRES-DOE reanalysis only assimilates surface pressure, and uses observed SST and sea-ice. We thus analyze the NOAA-CIRES-DOE in comparison with AMIP6 runs. We use 6-hourly data from JRA-55, NCEP2 and ERA5, and daily data from Era-Interim and NOAA-CIRES-DOE of zonal and meridional winds, temperature, specific humidity and geopotential over the 1979-2018

period; the NOAA-CIRES-DOE (20CRv3.MO) is available over the 1981-2015 period.

CESM

We also make use of the Community Earth System Model (CESM) large ensemble³³, which comprises 40 members running from 1920-2100 under the historical (through 2005) and RCP8.5 (through 2100) forcings. Each member in the ensemble is initialized with a slightly different air temperature ($\mathcal{O}10^{-14}$), yielding distinct time evolution over the 20th and 21st centuries. Thus, the spread across the members represents the internal variability, while the ensemble mean the forced response to external forcings. Since daily data is not available from CESM for our analysis, we use monthly data of kinetic energy. Thus, the EKE is here defined as deviations from monthly mean.

Linear normal-mode instability analysis

For calculating the growth rates of mid-latitude eddies we follow previous studies^{22,45–49} and conduct a linear normal-mode instability analysis⁵⁰. For the growth rate that arise from the vertical structure of the flow (baroclinicity) we use the quasigeostrophic equations (simplified set of equations for the mid-latitude flow that include conservation of vorticity in the interior and of buoyancy in the vertical boundaries) linearized about a zonal mean state (represented by an overbar), which can be written (for simplicity in Cartesian coordinates) as follows,

$$\begin{aligned} \frac{\partial q'}{\partial t} + \bar{u} \frac{\partial q'}{\partial x} + \frac{\partial \psi'}{\partial x} \frac{\partial \bar{q}}{\partial y} &= 0, H_p < p < p_s \\ \frac{\partial}{\partial t} \frac{\partial \psi'}{\partial p} + \bar{u} \frac{\partial}{\partial x} \frac{\partial \psi'}{\partial p} - \frac{\partial \psi'}{\partial x} \frac{\partial \bar{u}}{\partial p} &= 0, p = H_p, p_s, \end{aligned} \quad (1)$$

where $q' = \nabla^2 \psi' + \Gamma \psi'$ is the eddy quasigeostrophic potential vorticity, $u' = -\frac{\partial \psi'}{\partial y}$ and $v' = \frac{\partial \psi'}{\partial x}$,

$\Gamma = \frac{\partial}{\partial p} \frac{f^2}{S^2} \frac{\partial}{\partial p}$, $S^2 = -\frac{1}{\bar{\rho} \theta} \frac{\partial \bar{\theta}}{\partial p}$ is static stability, θ is potential temperature, ρ is the density, $\frac{\partial \bar{q}}{\partial y} = \beta - \Gamma \bar{u}$

is the mean quasigeostrophic potential vorticity meridional gradient (the instability analysis is conducted locally for the mid-latitudes and hence the mean flow is only vertically dependent), β is the meridional derivative of the Coriolis parameter (f) and H_p is the tropopause height (defined, following the WMO, as the lowest level where the vertical temperature gradient crosses the 2 K km^{-1} value).

Eq. 1 can be written in the form of an eigenvalue problem by substituting a plane-wave solution, $\psi' = \text{Re} \hat{\psi}'(p) e^{i(kx - \omega t)}$, where $\hat{\psi}'$ represents the normal modes (the eigenvectors), k is the zonal wavenumber and ω is frequency (the eigenvalues). The resulting vertical eigenvalue problem is then solved for each year using the vertically dependent wintertime zonal mean mid-latitude fields (velocity, temperature, tropopause height), and we analyze the resulting fastest growth rate each year.

For the growth rate that arise from the meridional structure of the flow (barotropic) we use the linearized absolute vorticity ($\eta = \nabla^2 \psi + f$) equation for two-dimensional flow,

$$\frac{\partial \nabla^2 \psi'}{\partial t} + \bar{u} \frac{\partial \nabla^2 \psi'}{\partial x} + \frac{\partial \psi'}{\partial x} \frac{\partial \bar{\eta}}{\partial y} = 0, \quad (2)$$

where $\frac{\partial \bar{\eta}}{\partial y} = \beta - \frac{\partial^2 \bar{u}}{\partial y^2}$, and $\psi' = 0$ at the meridional boundaries. A plane-wave solution of the form, $\psi' = \text{Re} \hat{\psi}'(y) e^{i(kx - \omega t)}$, transforms Eq. 2 to an eigenvalue problem, only here, unlike in Eq. 1, the normal modes are a function of latitude. The latitudinally dependent wintertime vertically averaged (between 850 – 300 mb) zonal mean winds are used to solve the resulting eigenvalue problem each year.

Eady growth rate and MAPE

The Eady growth rate³⁷ is calculated as $\sigma_{\text{Eady}} = \frac{f \frac{\partial \bar{u}}{\partial z}}{N}$, where $\frac{\partial \bar{u}}{\partial z}$ is the mean zonal wind shear

and $N^2 = \frac{g}{\bar{\theta}} \frac{\partial \bar{\theta}}{\partial z}$ is static stability. The Eady growth rate is averaged over the mid-latitudes and the extratropical troposphere (850 – 300 mb). The mean available potential energy (MAPE) is calculated as $\frac{c_p}{2g} \int \gamma \left(\overline{T^2} - \tilde{T}^2 \right) dp^{51}$, where $\gamma = \frac{-\kappa \bar{\theta}}{pT} \left(\frac{\partial \tilde{\theta}}{\partial p} \right)^{-1}$ and tilde represents a mean over the mid-latitudes at constant pressure. MAPE is integrated over the mid-latitude troposphere.

Data Availability: The data used in the manuscript is publicly available for CMIP6 data (<https://esgf-node.llnl.gov/projects/cmip6/>), NCEP (<https://psl.noaa.gov/>), JRA55 (<https://rda.ucar.edu/>), ERA-I and ERA5 (<https://www.ecmwf.int>), NOAA-CIRES-DOE (<https://www.psl.noaa.gov>) and CESM (<https://www.cesm.ucar.edu/projects/community-projects/LENS/data-sets.html>).

Code Availability: Any codes used in the manuscript are available at <https://doi.org/10.5281/zenodo.6434217>.

Methods references

40. Kobayashi et al., S. The JRA-55 Reanalysis: General specifications and basic characteristics. *J. Meteor. Soc. Japan* **93**, 5–48 (2015).
41. Kanamitsu, M. *et al.* Ncep-doe amip-ii reanalysis (r-2). *Bull. Am. Meteor. Soc.* **83**, 1631–1643 (2002).
42. Dee et al., D. P. The ERA-Interim reanalysis: configuration and performance of the data assimilation system. *Q. J. R. Meteorol. Soc.* **137**, 553–597 (2011).
43. Slivinski et al., L. C. Towards a more reliable historical reanalysis: Improvements for version 3 of the Twentieth Century Reanalysis system. *Q. J. R. Meteorol. Soc.* **145**, 2876–2908 (2019).
44. Hersbach et al., H. The era5 global reanalysis. *Quarterly Journal of the Royal Meteorological Society* **146**, 1999–2049 (2020).
45. Chemke, R. & Kaspi, Y. The latitudinal dependence of atmospheric jet scales and macroturbulent energy cascades. *J. Atmos. Sci.* **72**, 3891–3907 (2015).
46. Chemke, R. & Kaspi, Y. The effect of eddy-eddy interactions on jet formation and macroturbulent scales. *J. Atmos. Sci.* **73**, 2049–2059 (2016).
47. Chemke, R. & Kaspi, Y. The latitudinal dependence of the oceanic barotropic eddy kinetic energy and macroturbulence energy transport. *Geophys. Res. Lett.* **43**, 2723–2731 (2016).
48. Chemke, R., Dror, T. & Kaspi, Y. Barotropic kinetic energy and enstrophy transfers in the atmosphere. *Geophys. Res. Lett.* **43**, 7725–7734 (2016).

49. Chemke, R. Atmospheric energy transfer response to global warming. *Q. J. R. Meteorol. Soc.* **143**, 2296–2308 (2017).
50. Chemke, R. *Codes for calculating the eddy growth rate* (Zenodo, <https://doi.org/10.5281/zenodo.6434217>, 2022).
51. Peixoto, J. P. & Oort, A. H. *Physics of Climate* (American Institute of Physics, 1992).

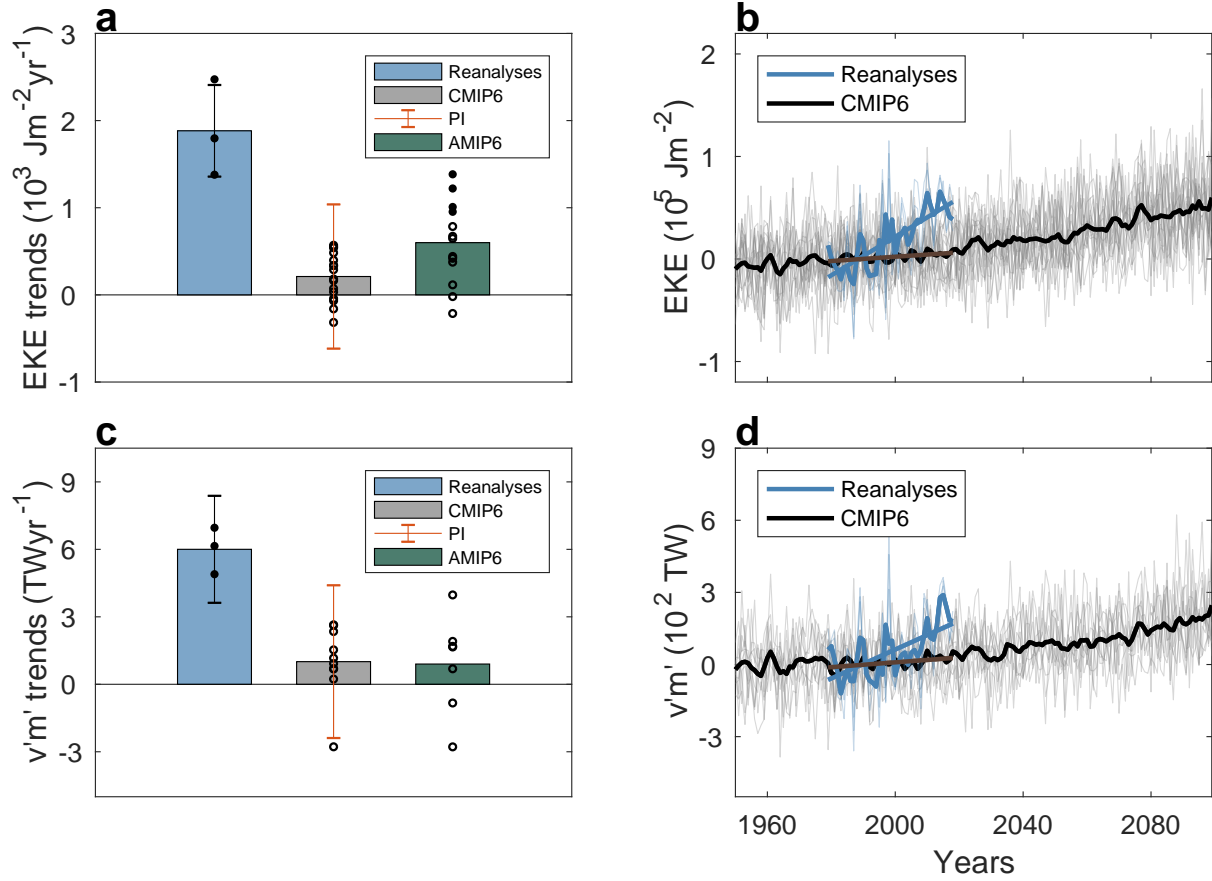


Figure 1: **Recent changes in Southern Hemisphere winter mid-latitude storm tracks.** The 1979-2018 trends in **a**, EKE and **b**, $v'm'$ in reanalyses mean (blue) and CMIP6 mean (gray). The green bars show the AMIP6 mean trends over the 1979-2014 period. The black circles show the trends from the individual reanalyses/models, where filled (open) circles show trends that are (not) statistically significant at the 5% level based on a Student's t-test. The black bars show the 95% confidence interval of the mean reanalyses trend and red bars show the two standard deviation across all 40-year trends from pre-industrial runs. Time evolution of **b**, EKE and **d**, $v'm'$, relative to the 1980-1999 period, in reanalyses mean (blue) and CMIP6 mean (black). Thin lines show the evolution of individual reanalyses/models. The ensemble mean time evolution is smoothed with a 3-point running mean for plotting purposes. Blue and brown lines show the 1979-2018 linear regressions in reanalyses and CMIP6 mean, respectively. The $v'm'$ trends are shown for 50°S , but similar results are evident throughout the mid-latitudes (Extended Data Fig. 2).

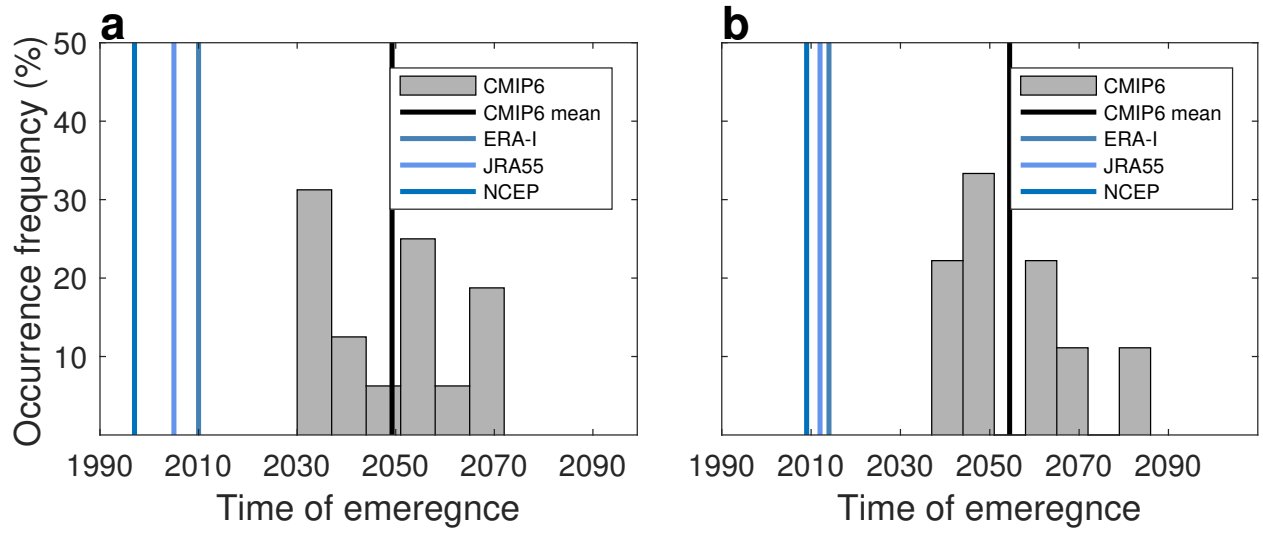


Figure 2: **Time of emergence of mid-latitude storm tracks.** The occurrence frequency of the time of emergence of **a**, EKE and **b**, $v'm'$ across the CMIP6 models (gray). The vertical blue and black lines show the emergence in each reanalysis (different shades of blue) and in CMIP6 mean, respectively.

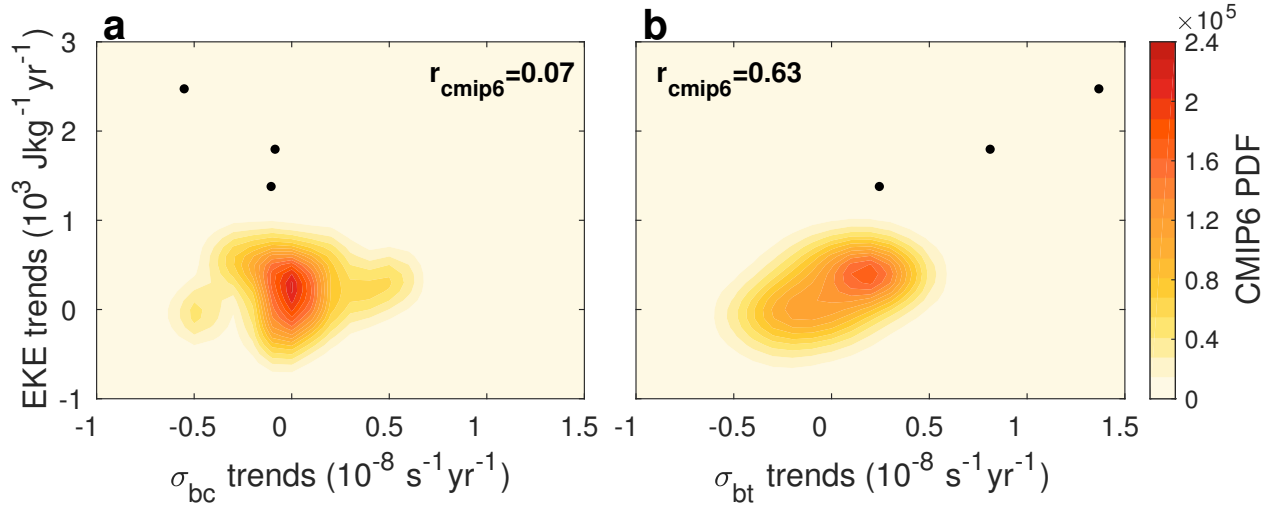


Figure 3: **Linear normal-mode instability analysis.** The 1979-2018 EKE trends plotted against the trends in growth rates of mid-latitude eddies, calculated from a linear normal-mode instability analysis, using the **a**, vertical (baroclinic, σ_{bc}) and **b**, meridional (barotropic, σ_{bt}) structure of the mean flow. Contours show the two-dimensional probability density function of the trends in CMIP6 models, estimated by fitting a kernel distribution (the area under each distribution is one), and the correlation appears in each panel. The black circles show the trends from reanalyses.

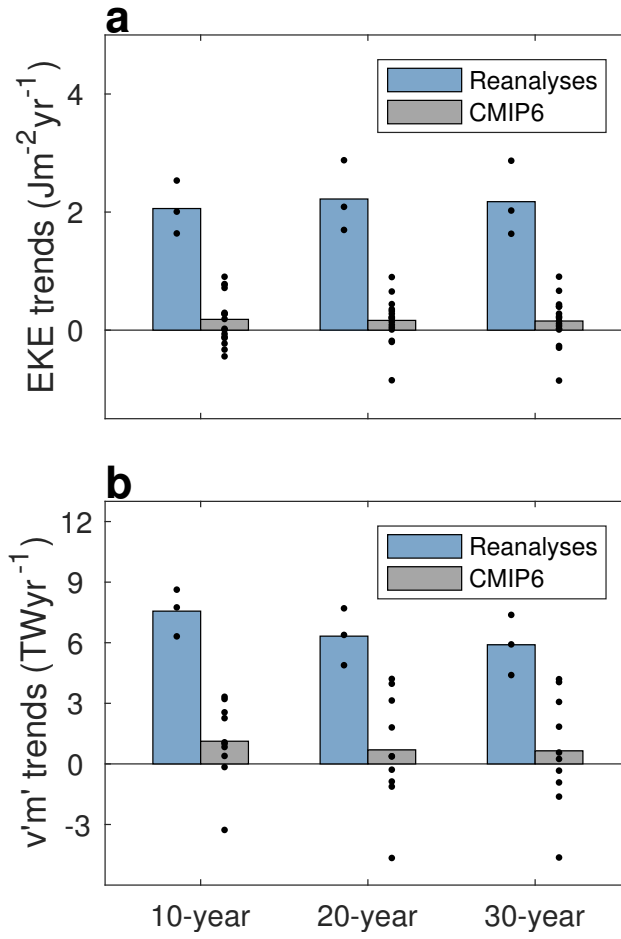
Extended Data for ”The intensification of winter mid-latitude storm tracks in the Southern Hemisphere”

Rei Chemke¹ & Yi Ming² & Janni Yuval³

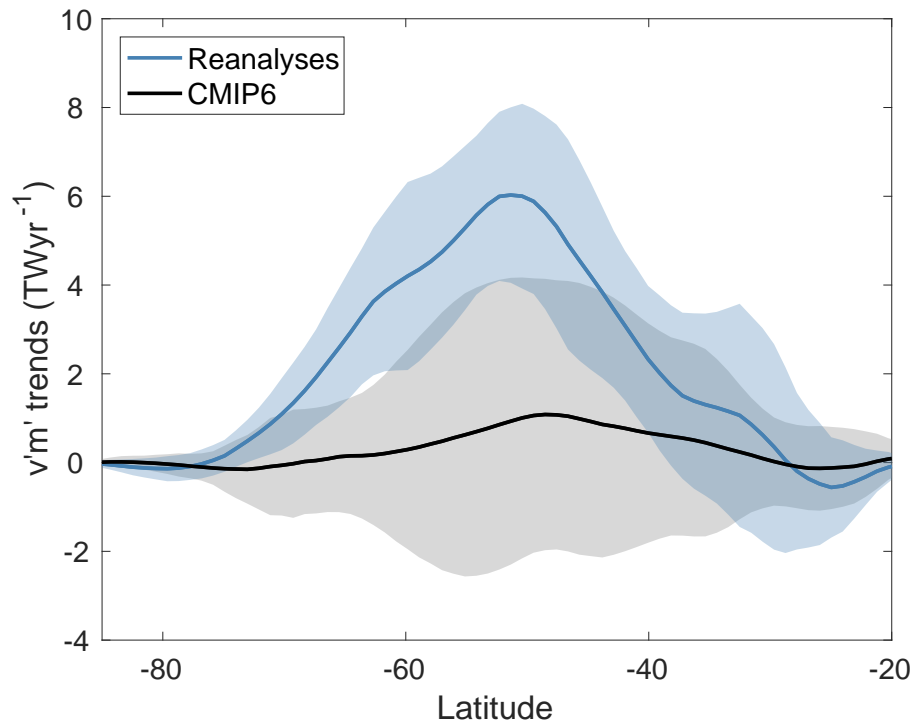
¹*Department of Earth and Planetary Sciences, Weizmann Institute of Science, Rehovot, Israel*

²*NOAA/Geophysical Fluid Dynamics Laboratory, Princeton, New Jersey, USA*

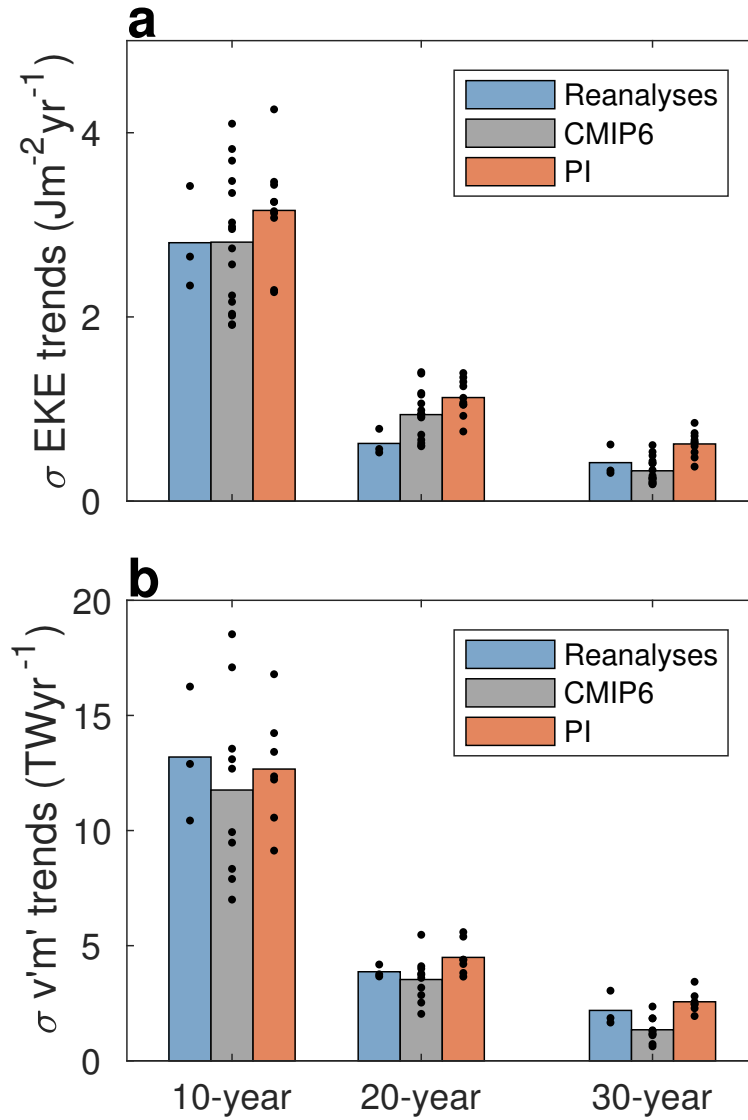
³*Department of Earth, Atmospheric and Planetary Sciences, MIT, Cambridge, Massachusetts, USA*



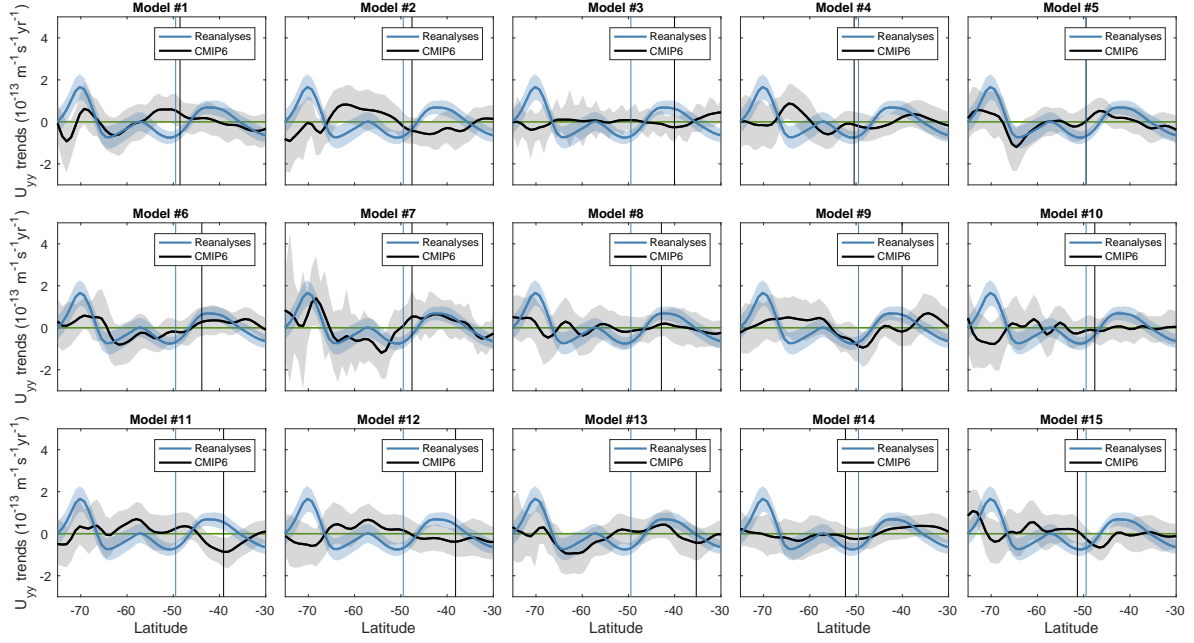
Extended Data Figure 1. The mean of all 10-year, 20-year and 30-year trends over the 1979-2018 period in **a**, eddy kinetic energy and **b**, poleward eddy moist static energy flux in reanalyses mean (blue) and CMIP6 mean (gray). The black circles show the trends from the individual reanalyses/models.



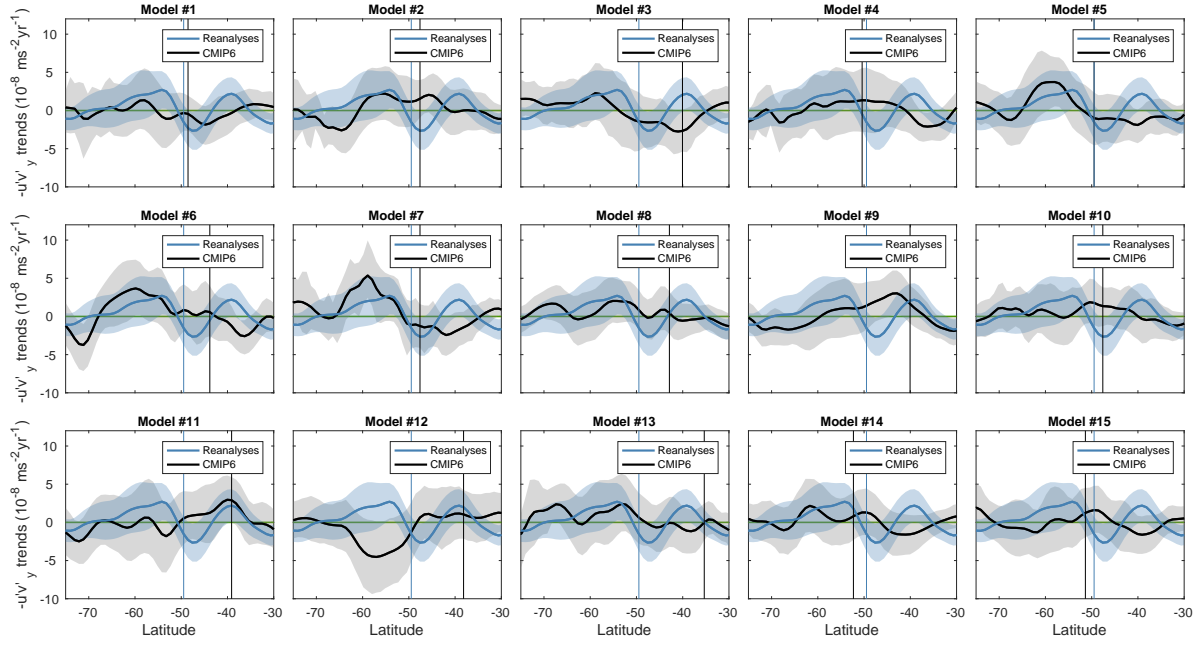
Extended Data Figure 2. The 1979-2018 trends in poleward eddy moist static energy flux as a function of latitude in reanalyses mean (blue line) and CMIP6 mean (black line). Shadings show two standard deviations across reanalyses/CMIP6 models.



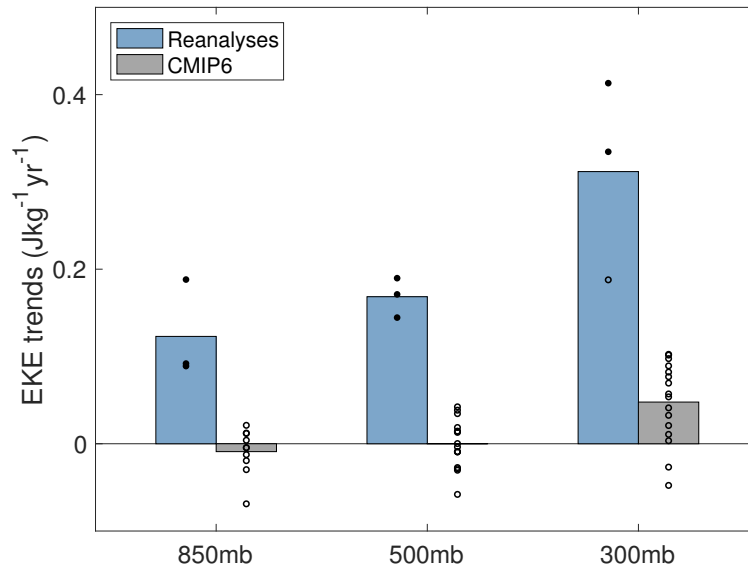
Extended Data Figure 3. One standard deviation across all 10-year, 20-year and 30-year trends in **a**, eddy kinetic energy and **b**, poleward eddy moist static energy flux in reanalyses mean (blue), CMIP6 mean (gray), and pre-industrial runs (red). The trends in CMIP6 and reanalyses were calculated over the detrended 1979-2018 period. The black circles show the results from individual reanalyses/models.



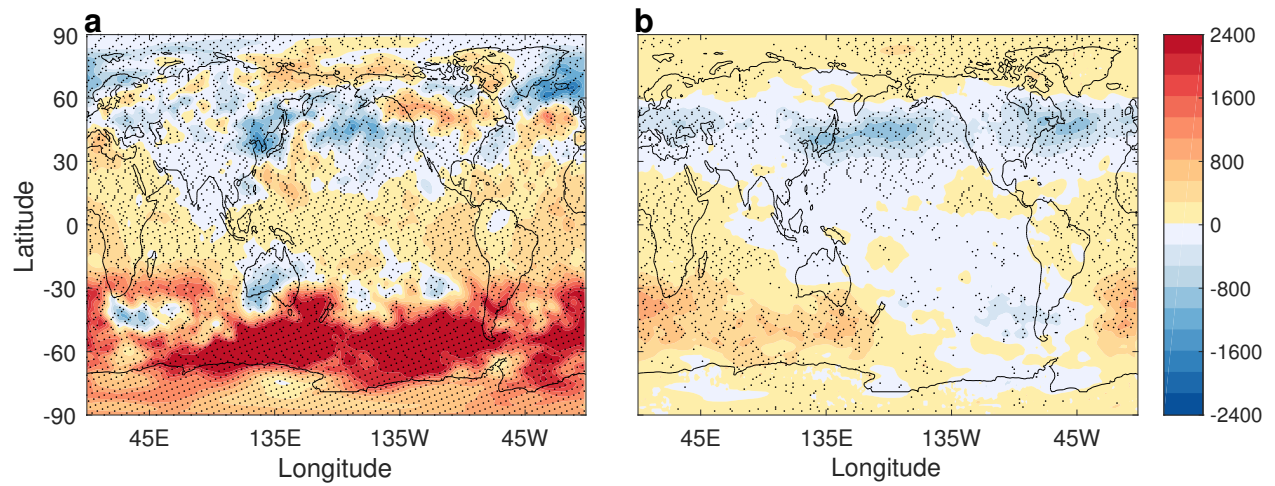
Extended Data Figure 4. The 1979-2018 trends in the second meridional derivative of the tropospheric (averaged between 850mb – 300mb) mean zonal wind, $\frac{\partial}{\partial \phi} \frac{1}{r \cos \phi} \frac{\partial \bar{u} \cos \phi}{\partial \phi}$, in mean reanalyses (blue lines) and CMIP6 models (black lines). Shadings show the 95% confidence interval of the trends. The vertical lines mark the climatological position of the mean zonal wind's core in reanalyses mean (blue) and CMIP6 models (black). Green line marks the zero line. The latitudinal structure is smoothed with a 3-point running mean for plotting purposes.



Extended Data Figure 5. The 1979-2018 trends in vertically averaged eddy momentum flux convergence, $-\frac{1}{r \cos^2 \phi} \frac{\partial \overline{u'v'} \cos^2 \phi}{\partial \phi}$, in mean reanalyses (blue lines) and CMIP6 models (black lines). Shadings show the 95% confidence interval of the trends. The vertical lines mark the climatological position of the mean zonal wind's core in reanalyses mean (blue) and CMIP6 models (black). Green line marks the zero line. The latitudinal structure is smoothed with a 3-point running mean for plotting purposes.



Extended Data Figure 6. The low-level (850mb), mid-level (500mb) and high-levels (300mb) 1979-2018 trends eddy kinetic energy in reanalyses mean (blue) and CMIP6 mean (gray). The black circles show the trends from the individual reanalyses/models, where filled (open) circles show trends that are (not) statistically significant at the 5% level based on a Student's t-test.



Extended Data Figure 7. The distribution of the 1979-2018 eddy kinetic energy trends in **a**, reanalyses mean and **b**, CMIP6 mean. The small black dots indicate regions where two thirds of the models/reanalyses agree on the sign.